JOURNAL OF GEOPHYSICAL RESEARCH, VOL. 113, D19201, doi:10.1029/2007JD009722, 2008

Spatial and temporal dependence of clouds and their radiative impacts on the large-scale vertical velocity profile

Jian Yuan[1] and Dennis L. Hartmann[1]

Received 17 December 2007; revised 20 March 2008; accepted 27 June 2008; published 1 October 2008.

[1] The structure of tropical large-scale vertical velocity from the European Centre for Medium-Range Weather Forecasts Re-Analysis is compared with simultaneous satellite measurements of precipitation, top of atmosphere radiation, and clouds from the Tropical Rainfall Measuring Mission (TRMM) on timescales ranging from hours to months. The first two empirical orthogonal functions of the vertical velocity profile represent the traditional deep circulation (PC1) and a shallower circulation (PC2) associated with middle-level divergence. Together they explain 90% of total variance and can distinguish two types of upward and downward motion: "top heavy" and "bottom heavy." Cloud and radiation budget quantities measured on TRMM have coherent relationships to PC1 and PC2 on all timescales from simultaneous to long-term means. The relative importance of PC2 is greater on short temporal and small spatial scales. "Top heavy" ascent is associated with deep cloud systems, more intense precipitation, lower outgoing long-wave radiation, stronger cloud long-wave forcing, and extensive anvils. Cloud short-wave forcing depends primarily on PC1, while the net cloud forcing depends more on PC2. High-thin clouds are less correlated with short-term variations of the vertical velocity. Shallow precipitation measured by TRMM precipitation radar is associated with "bottom heavy" upward motion. Temporal compositing with respect to intense precipitating events shows that strong upward motions tend to develop in the lower atmosphere first and then change to the more "top heavy" type of upward motion. The associated cloud systems show consistent temporal changes in which high-thick clouds develop first and extensive anvil clouds develop later. These results suggest that the elevated latent heating from stratiform precipitation and the development of "top heavy" upward motion profiles in the tropics are related to each other. The coherent relationships shown here between large-scale vertical velocity and independently measured cloud and precipitation data can be used to test the performance of climate models.

Citation: Yuan, J., and D. L. Hartmann (2008), Spatial and temporal dependence of clouds and their radiative impacts on the large-scale vertical velocity profile, *J. Geophys. Res.*, *113*, D19201, doi:10.1029/2007JD009722.

1. Introduction

[2] Cloud radiative feedback (CRF) stands as a large source of uncertainty in predicting future climate [*Cess et al.*, 1989; *Intergovernmental Panel on Climate Change*, 2007; *Stephens*, 2005]. Previous studies have shown that CRF is often coupled with the large-scale circulation, which affects both the amount and type of cloud present [*Dhuria and Kyle*, 1990; *Hartmann et al.*, 2001, 1992; *Ockert-Bell and Hartmann*, 1992]. Some efforts have been made to isolate the effect of large-scale circulation on clouds by using the large-scale vertical pressure velocity at 500 mbar, ω_{500}, as in the work of *Bony et al.* [2004] and *Williams et al.* [2003]. Compositing cloud properties with respect to ω_{500} provides a useful process-based diagnostic tool for climate model evaluation/intercomparison [*Wyant et al.*, 2006]. However, cloud properties can vary significantly even after vertical velocity and SST are accounted for [*Yuan et al.*, 2008].

[3] In the past three decades many studies have used radar and sounding measurements to investigate convective systems over tropical oceans. Stronger lower level upward vertical motion and a middle-level maximum of horizontal divergence associated with convective systems have been found from Global Atmospheric Research Program Atlantic Tropical Experiment (GATE, eastern Atlantic) compared to Marshall Islands (western Pacific) soundings [e.g., *Reed and Recker*, 1971; *Thompson et al.*, 1979]. GATE convective systems are found to have relatively more heating at lower troposphere compared to oceanic convection of Australia Monsoon Experiments (AMEX) [*Frank and McBride*, 1989]. Moreover, more lower clouds (defined by echo top heights) have been found from GATE compared to that from Tropical Ocean Global Atmosphere Coupled Ocean–Atmosphere Response Experiment (COARE)

[1]Department of Atmospheric Sciences, University of Washington, Seattle, Washington, USA.

0148-0227/08/2007JD009722$09.00

[*Johnson et al.*, 1999]. Recently, statistical results based on a large sample of satellite observations suggest that net cloud forcing over the eastern Pacific ITCZ is more negative because anvil and thin cloud abundances are less in the East than the western tropical Pacific [*Hartmann et al.*, 2001; *Kubar et al.*, 2007]. On the other hand, different types of large-scale vertical motion profiles associated with different types of circulation have been found over the western Pacific warm pool and the eastern Pacific ITCZ regions from reanalyses and ship sounding data [*Back and Bretherton*, 2006; *Trenberth et al.*, 2000; *Zhang et al.*, 2004]. Monthly mean satellite data and reanalyses also show that the anomalous cloud structure over the convective region in the western Pacific warm pool in 1998 is associated with the anomalous large-scale vertical velocity profiles [*Yuan et al.*, 2008].

[4] In the tropical atmosphere the adiabatic heating (generated by large-scale vertical motion) and the diabatic heating (latent heating, radiative heating etc.) associated with tropical convection are the major terms in the large-scale energy budget. Tropical mesoscale convective systems can alter the shape of the large-scale vertical motion profile by producing different types of latent heating profiles [*Houze*, 1982, 1989]. *Houze* [1982] argued that the stratiform heating (upper atmosphere heating and lower atmosphere cooling) generated by precipitating anvil clouds results in an elevated heating profile. This elevated heating profile can induce stronger large-scale upward motions in the upper troposphere [*Hartmann et al.*, 1984; *Lin et al.*, 2004; *Schumacher et al.*, 2004], which may be related to the "top heavy" type of upward motion profile. Radar observations and rawinsonde analysis suggest the existence of precipitating clouds with cloud top heights between traditional shallow cumulus and deep cumulonimbus categories, which are associated with the middle-level divergence (i.e., the "bottom heavy" type upward motion) [*Folkins et al.*, 2008; *Johnson et al.*, 1999]. *Zhang et al.* [2004] also hypothesize that the shallower convection over the east Pacific ITCZ might be responsible for the broad middle-level meridional return flow from warm SST region toward cold SST region.

[5] *Pandya and Durran* [1996] showed that gravity waves generated by vertically tilted convective thermal forcing from a squall-line system can produce consistent mesoscale circulation patterns compared with observations, and that gravity wave responses lead the changes in anvil cloud coverage. This suggests that anvil clouds might be associated with the time-variant synoptic/convective forcing, either externally applied or generated by the self-aggregation of the convection itself, which might not be captured by climatological mean properties of thermodynamics and dynamics (SST and omega etc.).

[6] These findings suggest a relationship between cloud population and the vertical structure of the large-scale vertical velocity. The characteristics of the vertical velocity (or divergence) profile of convective systems have been investigated on the basis of accurate in situ measurements or numerous convective clusters simulations [e.g., *Houze*, 1982, 1989; *Mapes and Houze*, 1995]. However, since convection varies from case to case, it is hard to obtain a general observed relationship between vertical structure of large-scale dynamics and cloud properties well-suited for diagnosing/evaluating general circulation models based on limited samples from field observations. Observational studies of cloud effects and vertical motions to date have been mostly done with monthly mean data or longer periods and focus on the midtroposphere vertical velocity. The short-term (daily or shorter) dependence of cloud radiative impacts on the vertical velocity profile has not been well documented. Considering the transient nature of convective activity, the short-term or high-frequency response is of great interest. Here we investigate the existence of coherent relationships on a variety of timescales and space scales between the European Centre for Medium-Range Weather Forecasts Re-Analysis (ERA-40) vertical velocity profiles and cloud, radiation, and precipitation data measured from satellites.

[7] Data used in this study are introduced in section 2. In section 3, the first two modes of vertical velocity profiles are analyzed. The dependence of clouds and their radiative impacts on large-scale vertical velocity profiles for different timescales are shown in section 4. The time dependence of vertical velocity profiles and clouds relative to precipitating events is presented in section 5, with conclusions and summary in section 6.

2. Data and Gridding

2.1. Data

[8] The Clouds and the Earth's Radiant Energy System (CERES) [*Wielicki et al.*, 1996] measures the broadband radiation at the top of the atmosphere. CERES instruments were launched aboard the Tropical Rainfall Measuring Mission (TRMM) in November 1997 and on the EOS Terra and Aqua satellites in 1999 and 2002. CERES instruments are substantially improved over the ERBE instruments. The CERES-TRMM-ES4 (1998) ERBE-like gridded daily top of atmosphere (TOA) radiant fluxes are used in this study [*Doelling et al.*, 2006]. The daily averaged outgoing long-wave radiation (OLR), total reflected solar radiation (TRS), and cloud radiative forcing at the top of the atmosphere are available. The long-wave, short-wave, and net cloud forcings are defined as

$$\mathrm{LWCF} = \mathrm{OLRcs} - \mathrm{OLR}, \tag{1}$$

$$\mathrm{SWCF} = \mathrm{TRScs} - \mathrm{TRS}, \tag{2}$$

$$\mathrm{NetCRF} = \mathrm{LWCF} + \mathrm{SWCF}, \tag{3}$$

where subscript "cs" indicates the clear sky value. The net radiation used in study is defined as

$$\mathrm{Net} = \mathrm{Inc} - \mathrm{TRS} - \mathrm{OLR}, \tag{4}$$

where the "Inc" is the incoming solar radiation at the TOA.

[9] Cloud information is obtained from the CERES-TRMM-SSF product. Cloud properties are inferred from the simultaneous measurements by the Visible Infrared Scanner (VIRS) imager, which flies along with CERES on the TRMM spacecraft. Since we are interested in both thermal and optical properties of tropical convective cloud

systems, only daytime cloud data are used. The main algorithm used during the daytime is the Visible Infrared Solar-Infrared Technique (VIST) [*Minnis et al.*, 1995]. The CERES cloud product provides cloud effective temperature and optical depth along with other microphysical/geometrical properties [*Minnis et al.*, 1999]. Comparisons between cloud properties from VIS and radar observations over the ARM southern Great Plains (SGP) site based on limited samples suggest that the VIRS and surface daytime retrievals agree within the CERES accuracy goals and at roughly same level as a similar comparison of surface, aircraft, and GOES retrievals for stratus over the same site [*Dong et al.*, 2002].

[10] Both the Tropical Rainfall Measuring Mission (TRMM) Precipitation Radar (PR) Rainfall Rate and Profile Product (TRMM2a25, version 6) [*Iguchi et al.*, 2000] and the merged high-quality (HQ)/infrared (IR) precipitation data (TRMM3b42, version 6) are used in this study. The TRMM-PR operates at 13.8 GHz that measures the 3-D rainfall distribution and provide the most accurate rain rate profile covering the whole tropics measured from space. The estimates of attenuation-corrected radar reflectivity factor and near-surface rainfall rate are given at each resolution cell (4 km $\times$ 4 km $\times$ 250 m) of the PR. The rain type information from TRMM PR Rain Characteristics Product (TRMM2a23) [*Awaka et al.*, 1997] is included in the current version of TRMM2a25.

[11] TRMM3b42 is a mutisatellite and rain gauge analysis based global precipitation product [*Huffman et al.*, 1997, 1995]. It provides precipitation data and root-mean-square (RMS) precipitation-error estimates [*Huffman*, 1997] gridded on a 3-h temporal resolution and a 25 km spatial resolution in a global belt extending from 50 degrees south to 50 degrees north latitude. The 3b42 estimates combine the high-quality (HQ) microwave estimates that are calibrated by TRMM PR data and the variable rain rate (VAR) IR estimates created by using the calibrated microwave precipitation. The precipitation field is rescaled on the basis of the GPCP One-Degree Daily combination data set by scaling the short-period estimates to sum to a monthly estimate that includes monthly gauge data.

[12] The European Centre for Medium-Range Weather Forecasts (ECMWF) Re-Analysis (ERA-40) is used in this study to characterize the vertical velocity field. The ERA-40 project is a comprehensive global analysis for the 45-year period covering September 1957 to August 2002 [*Uppala et al.*, 2005]. Multiple archives of in situ and satellite observations were assimilated by the model. The data used here are the ECMWF ERA-40 model output of the vertical pressure velocity on 13 constant pressure surfaces (ranging from 1000 hPa to 70 hPa). The vertical velocities are archived at global T159 spectral resolution in spherical harmonics and extracted to the reduced N80 Gaussian grid with an approximate horizontal resolution of 125 km. All data are archived 4$\times$ daily at 00z, 06z, 12z and 18z.

2.2. Gridding

[13] All data used for compositing study are linearly regridded/averaged into $1^\circ \times 1^\circ$ spatial resolution. CERES-TRMM-PFM-ES4 daily TOA radiation and cloud radiative forcing data are provided at $2.5^\circ \times 2.5^\circ$ resolution. ERA-40 vertical velocities have $1.125^\circ \times 1.125^\circ$ resolution. They are both regridded to $1^\circ \times 1^\circ$ resolution. TRMM3b42 has $0.25^\circ \times 0.25^\circ$ resolution and it is averaged to $1^\circ \times 1^\circ$ resolution. CERES-SSF cloud data and TRMM2a25 PR data are provided as satellite granule data with footprint resolution of 4$\sim$10 km. They are averaged into $0.25^\circ \times 0.25^\circ$ grids at first and then re-averaged to $1^\circ \times 1^\circ$ grids. Quality control flags have been considered during the regridding process. Grids with few samples (i.e., footprints or subgrids covering less than 2/3 of the averaging grids) are not used in this study. Since daily clear sky TRS are sparse and unavailable more over convective areas, the monthly mean clear sky albedo data are used with daily insolation to generate the clear sky TRS for grids without valid data. For this reason the SWCF temporal variations are not evaluated in the high-frequency analysis (periods shorter than 5 days).

[14] To study the dependence on timescales, temporal averaging is performed on varying intervals. For the compositing study, all data are first daily averaged, because the TOA radiation is provided at this frequency. Then longer time averages of these quantities are based on daily averages. For the study in section 5, CERES clouds and TRMM PR data are averaged to 3-h boxes, consistent with TRMM3b42. ERA-40 is left as 4xdaily to preserve the higher temporal resolution. The time period for the analysis is 8 months (January 1998 to August 1998) for all data in this study except for Figure 7, for which 2 years of PR data (1998–1999) were used. All analysis is over open water away from land.

3. Structure of the Vertical Velocity Profile

[15] To characterize the structure of the large-scale vertical velocity profile we perform empirical orthogonal function (EOF) analysis of the tropical vertical velocity profiles. Analysis is performed separately for instantaneous data and for data averaged over different time periods from 1 day to 1 month. To properly perform the EOF analysis, the pressure velocity at each level is weighted by multiplying by the layer thickness:

$$\omega_i^* = \omega_i (P_{i+1} - P_{i-1})/2, \tag{5}$$

where P_i, ω_i, and ω_i* refer to the pressure, the vertical pressure velocity, and the weighted vertical pressure velocity at the level i, respectively. The surface pressure is also used to properly estimate the weighting for the lowest level (1000 hPa). Then the EOF analysis is performed on the covariance matrix of ω*. When using equal-angle gridded data another weighting is added to take into account the area (square root of cosine[latitude] of each grid).

[16] Figure 1a shows the two leading EOFs (with weighting removed) of vertical velocity profiles based on different timescales. The 4$\times$daily data is averaged to different timescales to see how the resulting EOFs change with the timescale. All EOF analysis is based on $2.5^\circ \times 2.5^\circ$ gridded data over the whole tropics (30°N–30°S). The EOFs derived from 22 years of monthly mean data are also shown in Figure 1a. The EOFs change shape only slightly when data with different timescales are used. EOF1 shows a broad maximum through the middle troposphere, which is associated with the deep circulation mode with strong convergence/divergence in the upper and lower atmosphere. EOF2 shows

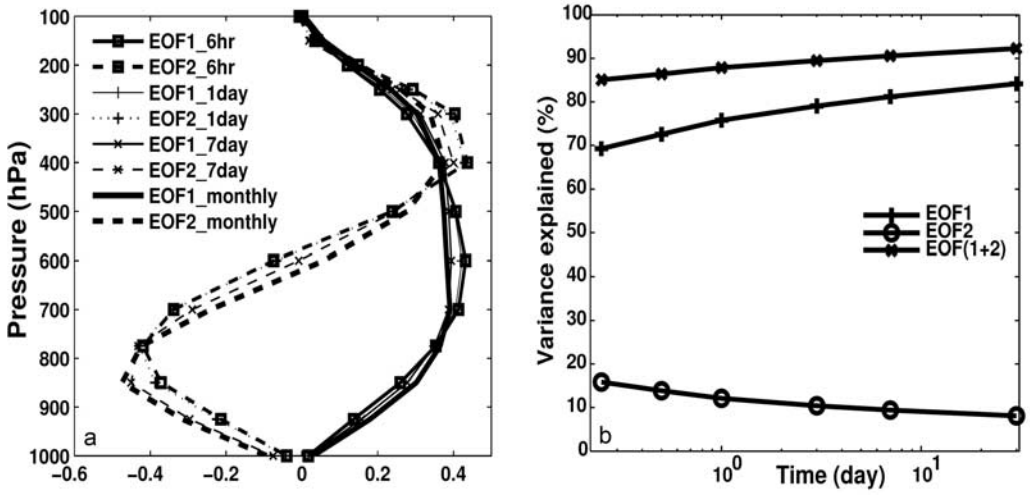

Figure 1. (a) EOF1 and EOF2 of the vertical velocity profile derived from the European Centre for Medium-Range Weather Forecasts Re-Analysis (ERA-40) and (b) the fraction of total variance explained by them, as a function of timescales.

a shift between the upper and lower atmosphere that corresponds to a broad middle atmosphere convergence/divergence corresponding to shallower circulations. All EOF1 and EOF2 are statistically distinct from each other and from higher modes (95% level), after taking into account autocorrelation following *Bretherton et al.* [1999]. By projecting EOF1 and EOF2 on the original vertical velocity data we can get the first two principle components PC1 and PC2. Using EOF1 and EOF2 derived on the basis of monthly mean data (Figure 1, thick solid and thick dashed lines) or 4xdaily data (Figure 1, solid line with squares and dashed line with squares) resulting PC1s have a correlation of 0.9996 (r^2 = 99.9%) with the regression 1.002(0.2% deviation). Resulting PC2s have a correlation of 0.986 (r^2 = 97.2%) with the regression 1.005 (0.5% deviation). Thus using different averaging periods to determine the EOFs has no effect on the PCs. The fraction of variance explained by EOF2 is greatest for instantaneous data and decreases with averaging period (Figure 1b), which indicates that the second mode is associated more with short-term variability. EOF1&2 together persistently explain (85%∼90%) of the total variance. Power spectral analysis of PC1 and PC2 (not shown) shows that about 80% of total variance is explained by periods longer than 5 days for PC1 and only about 50% for PC2. Since the internal mode PC2 has a slower gravity wave speed than PC1, it is likely that the smaller temporal and spatial scales of PC2 arise from the forcing that drives it. It is driven in the positive phase by shallow convection and in the negative phase by mature stratiform convection. It is likely that the slow radiative cooling of clear skies that balances most of the convective heating has a deep structure like PC1, and the response of the clear-sky cooling is likely to be slow, so this may also help to explain the difference in timescale between PC1 and PC2.

[17] Figure 2 shows the maps of annual mean PC1 and PC2 derived from ERA-40 based on 10 years of data. They are scaled by each EOF's amplitude. We define the EOFs' sign such that positive PC1 means downward motion. Positive PC2 means low-level upward motion and high-level downward motion, which corresponds to middle-level divergence. The magnitude of PC1 is scaled so that its value is nearly equivalent to the middle-troposphere pressure velocity. PC2's magnitude is scaled so that it is equivalent to the amplitude of the vertical change of velocity. The map of annual mean PC1 looks almost exactly like ω_{500} and so characterizes the typical mean tropical large-scale circulation pattern.

[18] The map of PC2 brings some new information in addition to PC1. It shows that over the eastern ITCZ PC2 has positive sign. As described by *Back and Bretherton* [2006], that constitutes the "bottom heavy" type of vertical motion profile. This is also consistent with the work of *Trenberth et al.* [2000] and *Zhang et al.* [2004] in that over the eastern Pacific ITCZ area, middle-level meridional overturning rises over the warm SST region. Over the western Pacific/Indonesian region the PC1 and PC2 are both negative ("top heavy" upward motion), which indicates a deep layer of convergence in the lower troposphere. These differences in the mean motion field are consistent with more stratiform elevated clouds in the western Pacific Ocean [*Houze*, 1982]. The middle-level overturning circulation over the east Pacific Ocean associated with the "bottom heavy" upward motion may be related to strong SST gradients [*Back*, 2007; *Zhang et al.*, 2004] and less upper level anvil clouds [*Kubar et al.*, 2007]. Our analysis is performed on the two rectangular regions, western Pacific (15°S–15°N, 100°E–160°E; WP hereinafter) the eastern pacific ITCZ area (15°S–15°N, 210°E–270°E; EP hereinafter). Only grid cells without land are included in the analysis, but if we include the land areas in the WP box the results are not very different.

[19] In this study we use EOF1 and EOF2 to characterize the vertical velocity profile and composite other cloud and radiation variables into a PC1 and PC2 phase space. The different types of vertical velocity profiles (or anomalies of

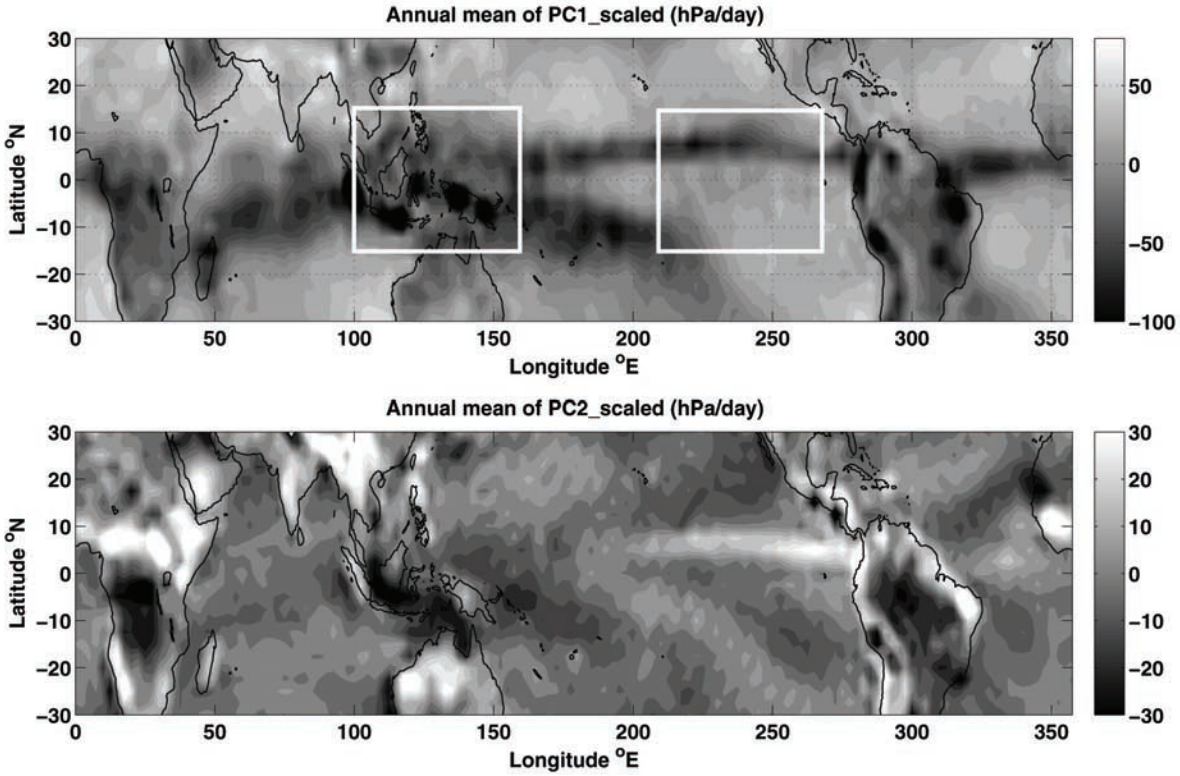

Figure 2. The averaged annual mean (1990–1999) map of PC1 and PC2 scaled by the amplitude of EOF1 and EOF2.

vertical velocity profiles) in the PC1-PC2 phase space are shown schematically in Figure 3. Quadrants 1 and 3 represent "bottom heavy" vertical motion, and quadrants 2 and 4 represent "top heavy" vertical motion.

4. Compositing Observations Into PC1-PC2 Coordinates

[20] The observed precipitation, TOA radiation and retrieved clouds are composited into bins defined by PC1 and PC2. We separate the compositing into two parts. First we compute the temporal anomalies from both reanalysis data and observations. These observed anomalies are then assigned to this array on the basis of these anomalies of PC1 and PC2. We will label these anomalies as δ_{PC1} and δ_{PC2}. This shows the relation of anomalies to temporal anomalies in PC1 and PC2. The second method uses the long-term mean of all the data to reflect the relations due to large-scale spatial dependence of climatology.

[21] In what follows we will show very consistent dependencies of cloud and radiation properties measured from satellites on the first two modes of vertical velocity from ERA-40 reanalysis. The consistent and physically reasonable results obtained here are somewhat surprising given the grid and time matching that must be done and the fact that the vertical velocities are not observed, but are inferred from a data assimilation process. Decomposing the vertical velocity profile into EOF structures reduces the noise in the vertical velocity profiles somewhat, but we believe the main reason we obtain these consistent results is that we average over a large amount of data for each result that we show. Averaging over a large ensemble of events allows the real dependencies to emerge from what might be a noisy data set. It may also be that the vertical velocities from reanalysis are better than many people think. We have performed these

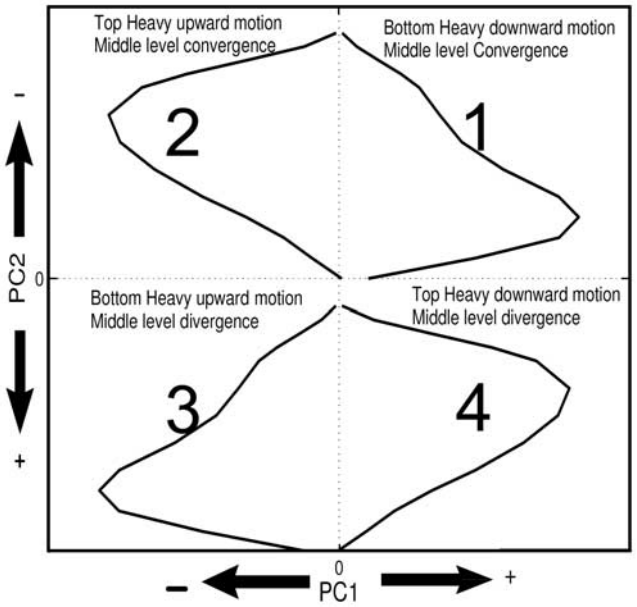

Figure 3. Schematic view of the signature types of vertical velocity profiles in different quadrants of the PC1 versus PC2 (or δPC1 and δ PC2) phase space used here. Quadrant numbers are shown at the center of each quadrant.

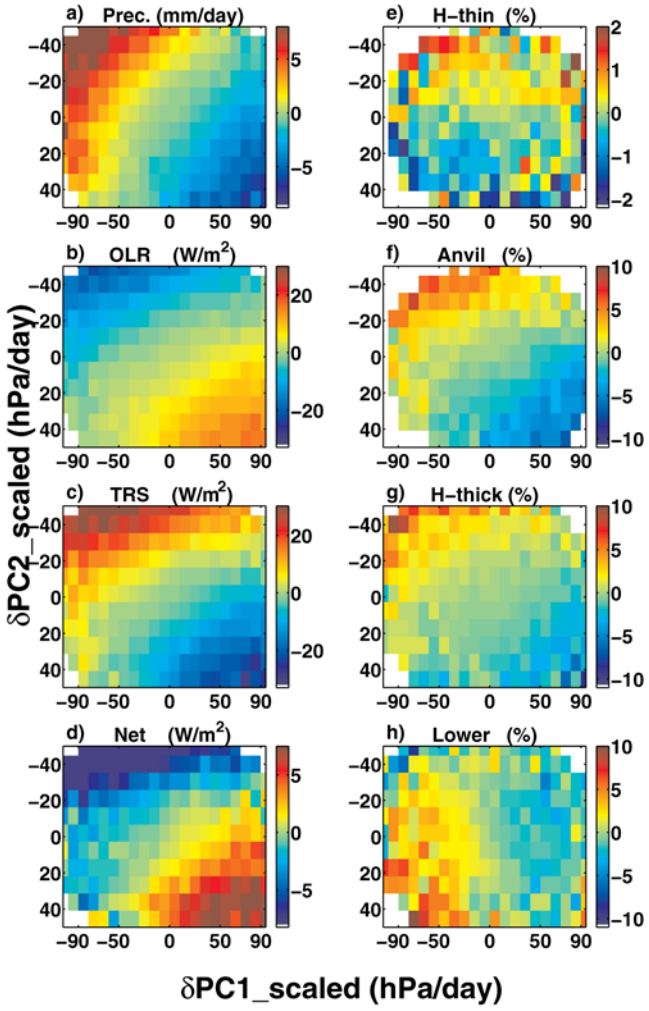

Figure 4. (a–h) Anomalies of precipitation, top of atmosphere radiative fluxes, and clouds composited into δPC1 and δPC2. The anomalies are daily mean departures from the 5-day running mean centering on that day. Domain used is western Pacific (WP), 15°S–15°N, 100°E–160°E. OLR, outgoing long-wave radiation; TRS, total reflected solar radiation.

analyses with NCEP/NCAR vertical velocities and obtained very similar results in all cases.

[22] Since most results are similar between the WP and EP, primarily only results of the WP area are shown in this paper. Because CERES-ES4 TOA radiation is provided as daily averages, all data are daily averaged. About 450,000 data grids are used for each area. We regroup CERES clouds into four cloud types following *Kubar et al.* [2007]. High clouds with cloud effective temperature less than 245°K are separated into three types. High-thin clouds are clouds with the visible optical thickness less than 4, which generally have positive cloud net radiative forcing. Anvil clouds are defined as clouds having visible optical thickness not less than 4 but smaller than 32. High-thick clouds with optical thickness greater than 32 are tightly associated with precipitation rate [*Kubar et al.*, 2007]. Since cloud retrievals are based on passive retrieving techniques measured from space, lower clouds usually have high anticorrelations with high clouds due to overlapping. For simplicity the lower clouds are grouped in one category defined as clouds with effective temperature higher than 245°K. Composites bins with less than 100 samples are left blank (white).

4.1. Composites Based on Anomalies

[23] From Figure 4 it is clear that on short timescales, TRMM daily precipitation and CERES daily TOA fluxes systematically change with both δ_{PC1} and δ_{PC2}. The steepest gradient occurs along the "top heavy" upward motion to the "top heavy" downward motion axis (i.e., along the 2–4 quadrant axis), which highlights the dependence on δPC2. Despite the fact that PC2 explains only about 15% of the daily variance of omega, it has a first-order effect on the radiation balance. Figure 4 shows consistent changes along this diagonal (quadrants 2–4) direction in precipitation (~15 mm/d), OLR (~45 W/m^2), TRS (~60 W/m^2), and LWCF (~45 W/m^2). Figure 4d suggests that more intense convection produces more negative net radiation, which tends to lower the sea surface temperature and inhibit convection. Because the long-wave effect and the short-wave effect of clouds tend to cancel each other, the change of the net radiation is relatively small (~15 W/m^2), but the reduction in net radiation at the surface would be much larger, closer to the change in absorbed solar (~50 W/m^2).

[24] Cloud information is shown in Figures 4e–4h. The cloud forcing is not shown because the LWCF primarily shows the same information as the OLR and the daily SWCF data is sparse in the high-frequency sample (see section 2). Generally clouds are consistent with Figure 4a. Anvil (~10% changes) and high-thick clouds (~10% changes) show similar dependence on vertical motions as precipitation and TOA measurements and seem more sensitive to PC2 than PC1. Although relatively abundant, high-thin clouds show little sensitivity to large-scale motions. This might be because high-thin clouds (cirrus) are only loosely related to convective activities [*Luo and Rossow*, 2004] and their lifetimes are much longer than convective events. The lower clouds are seen more frequently in the "bottom heavy" upward motion regime.

[25] Next we focus on longer timescale anomalies by taking the 5-day mean departures from 30-day means. Figure 5 shows similar information as Figure 4 but with slightly greater dependence on δ_{PC1}. On this longer timescale the SWCF sampling is better. SWCF shows weaker dependence on δ_{PC2} than LWCF. Hence the net cloud forcing is more sensitive to δ_{PC2} than δ_{PC1}. The long-wave effects depend more on the altitude of clouds but the short-wave effects depend more on the thickness of clouds. Strong lower level cloud formation (associated with middle-level divergence) may produce thick clouds with lower cloud top heights, which produce stronger negative cloud forcing. Figure 5k shows that over "top heavy" upward motion regimes the net cloud forcing is near zero and is about −10W/m^2 over "bottom heavy" areas. Anvil clouds (~20% changes) and high-thick (~10% changes) show similar dependence on vertical motions as precipitation and TOA radiation. The OLR (~60 W/m^2) and TRS (~75 W/m^2) show stronger contrast than in Figure 4. Since clouds last longer than precipitation, averaging over a longer period reduces the anomaly of the vertical motion

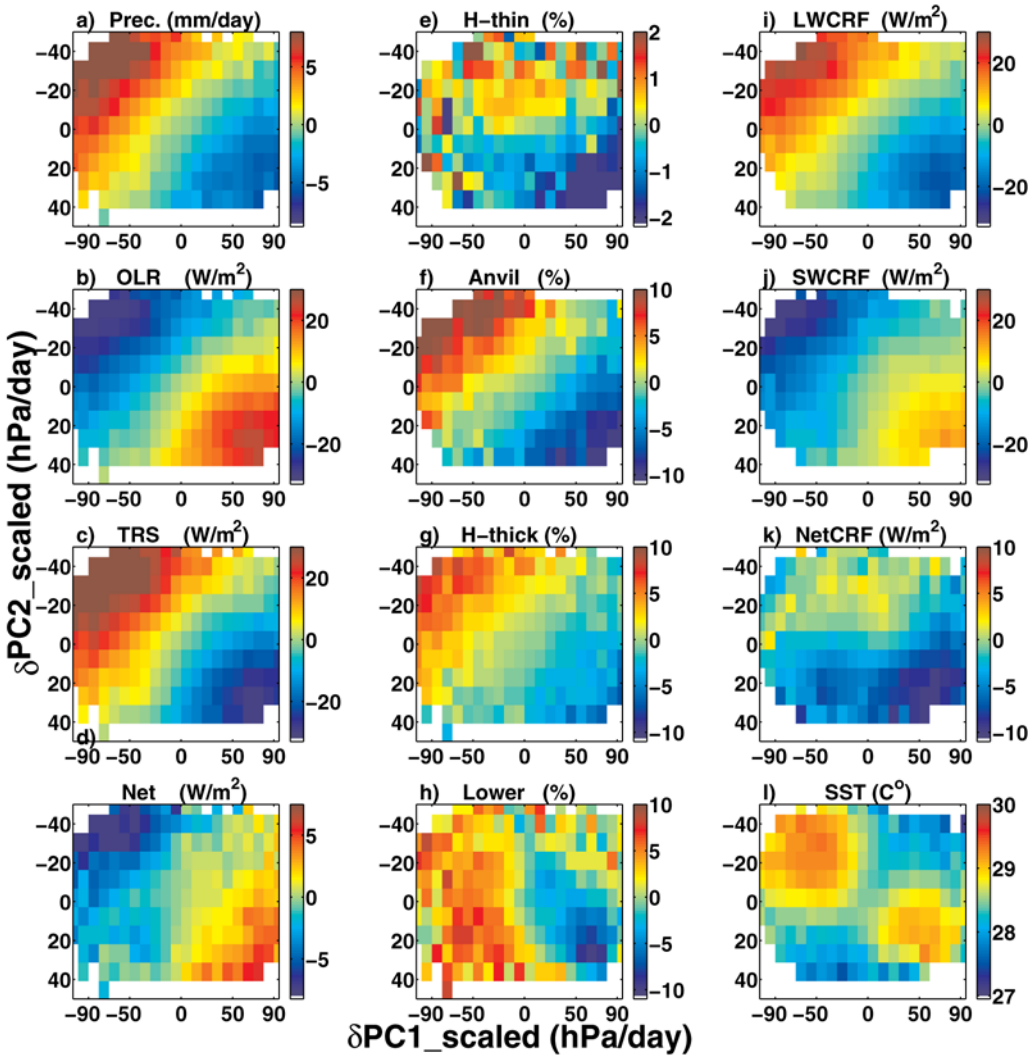

Figure 5. (a–l) Same as in Figure 4, but anomalies are 5-day mean departures from the 30-day running mean centered on the 5-day interval of interest. LWCRF, long-wave cloud radiative forcing; SWCRF, short-wave cloud radiative forcing; SST, sea surface temperature.

more than the cloud effects. So all variables related to clouds have stronger contrast as the timescales is increased from 1 day to 5 days. High-thin clouds (Figure 5i) show similar behavior as in Figure 4e. Figure 5h shows that lower clouds respond most strongly to PC1 but especially when the profile is "bottom heavy."

[26] The composite of the SST (not anomalies) in δ_{PC1} and δ_{PC2} coordinates is shown in Figure 5l. It shows that stronger upper atmosphere divergence (quadrants 2–4) happens over warm SST. Stronger contrast in the net radiation (Figure 5d) is associated with weak SST difference across the diagonal connecting quadrants 2–4. This suggests that deep convection over warm sea surface tends to reduce the net radiation reaching the surface by blocking more short-wave radiation, which in turn reduces the SST gradient over WP warm pool [*Hartmann et al.*, 2001; *Ramanathan and Collins*, 1991]. Stronger low-level convergence (1–3 quadrants) mostly happens over relatively cold SST areas, which are also areas with stronger SST gradients within the warm pool area. Similar results can be obtained from shorter timescale study (daily anomalies from 5-day mean). The EP (not shown) shows similar results as for the WP.

4.2. Composites Based on Long-Term Means

[27] We next use 30-day running mean data, so that the composites mainly reflect changes associated with spatial gradients of temporal means. Large inhomogeneities in the net downward radiation (Figure 6d) are present in these data. The composite of ERA-40 SST (Figure 6l) has a similar pattern as the net radiation, with high SST associated with high net radiation. In the most "top heavy" upward motion regime the net radiation is about 80∼100 W/m^2, and these regions correspond to regions of the warmest SST. For strongly "bottom heavy" upward motion regions, the net radiation is 40–60 W/m^2. The "top heavy" upward motion region corresponds to intense precipitation (10∼12 mm/d), extensive anvil clouds (15∼20%), more high-thick clouds (5∼10%), more high-thin clouds (7.5∼10%) and less lower clouds (∼40%). The dependence of the net radiation now has the opposite sign compared with anomaly studies (comparing Figure 6d with Figures 5d and 4d). This is

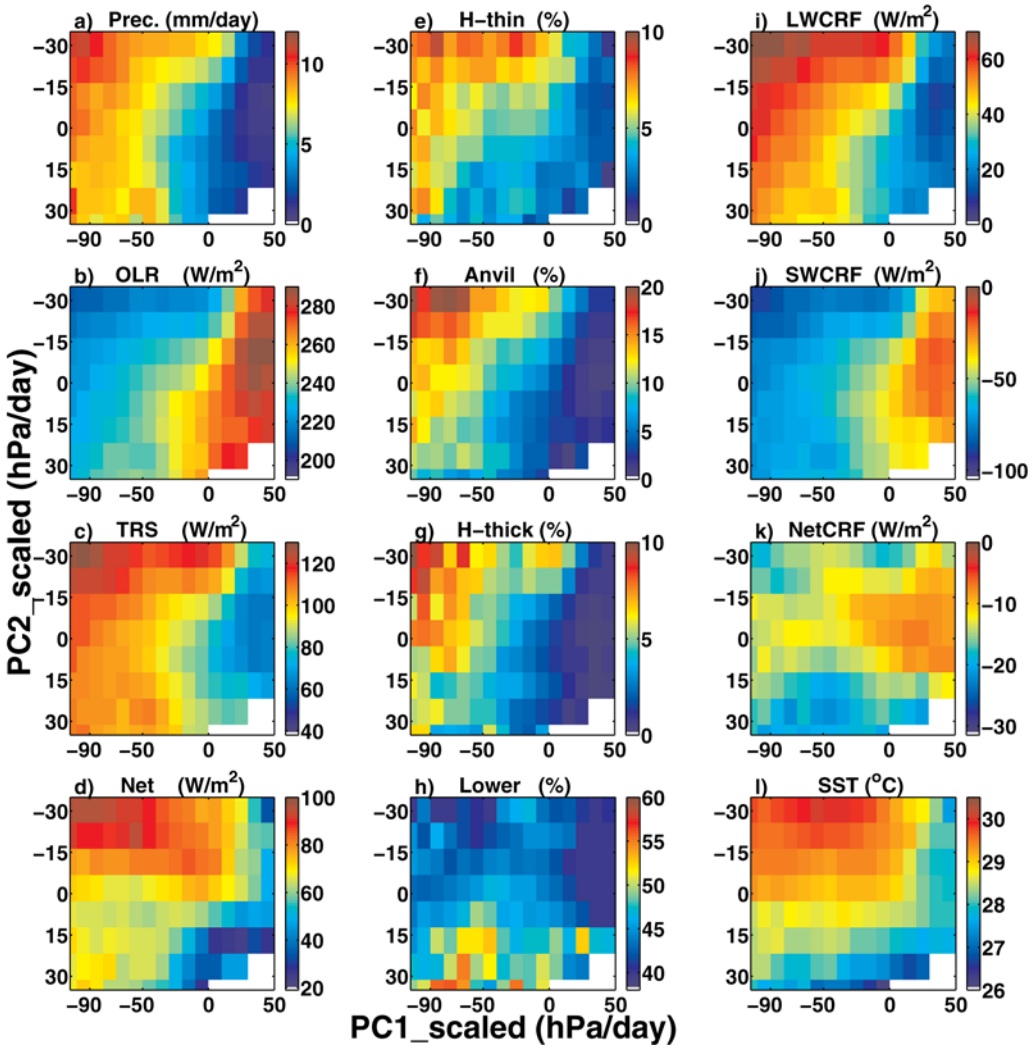

Figure 6. (a–l) Same as in Figure 4 but based on 30-day running mean values.

because in anomaly studies most of the net radiation changes are due to cloud changes. While for the long-term mean study, changes in the net radiation mainly result from the spatial variance of the incoming solar radiation, and the cancellation between long-wave and short-wave cloud forcing is more complete for longer timescales. Warm ocean areas receiving the most energy are the most active and produce more deep convection.

[28] Unlike in the anomaly studies shown previously, high-thin clouds (Figure 6e) now favor "top heavy" upward motion, which suggests that the high-thin cloud coverage significantly depends on large-scale dynamics rather than just convection [*Luo and Rossow*, 2004]. Stronger large-scale upward motion in the upper troposphere favors high-thin cloud formation and supports their longer lifetime.

[29] Precipitation, OLR, LWCF, anvil and high-thick clouds show similar dependence as in the anomaly studies, but show weaker dependence on PC2. Owing to the presence of high-thin clouds, LWCF and OLR look a bit different from anvil and high-thick clouds. Lower clouds (Figure 6h) over the "bottom heavy" upward motion regimes are about 10% (absolute fraction) more than in "top heavy" upward motion regimes. Short-wave effects (TRS and SWCF) only weakly depend on PC2 because more low clouds are present in "bottom heavy" upward motion regimes. The NetCRF depends both on PC1 and PC2 but is relatively more sensitive to PC2.

4.3. Relative Dependence on PC1 and PC2

[30] To quantitatively estimate the relative dependence of other variables on PC1 and PC2 we perform a linear regression based on the composited phase plots (Figures 4–6):

$$V' = A \cdot PC1' + B \cdot PC2', \tag{6}$$

where V refers to dependent variables. V', $PC1'$, and $PC2'$ (or $\delta_{PC1}{}'$ and $\delta PC2'$ for anomaly studies) are defined to have zero mean and unit variance. We use the values from boxes (joint bins) in the plot that have data and give them each equal weight, regardless of how many data points are used for the averages in each box. For each box we also have a pair of PC1 and PC2 corresponding to it. So we have a set of variables and PC1 and PC2 matched with each other. Then we remove their means and normalize them by dividing their standard deviations. Hence A and B based on

Table 1. Relative Dependence of Precipitation, TOA Radiative Fluxes, and Clouds on PC1 and PC2[a]

Variable	Correlation Coefficients	Derived From Figure 4 (Daily Anomalies)	Derived From Figure 5 (5-Day Anomalies)	Derived From Figure 6 (30-Day Means)
Precipitation	A	−0.73	−0.72	−0.92
	B	−0.62	−0.62	−0.25
OLR	A	0.50	0.67	0.86
	B	0.84	0.67	0.36
TRS	A	−0.50	−0.68	−0.83
	B	−0.83	−0.66	−0.30
Net	A	0.50	0.68	−0.72
	B	0.79	0.58	−0.50
High-thin clouds	A	(−0.01)	(−0.32)	(−0.66)
	B	(−0.45)	(−0.49)	(−0.54)
Anvil clouds	A	−0.53	−0.63	−0.80
	B	−0.79	−0.69	−0.39
High-thick clouds	A	−0.49	−0.66	−0.80
	B	−0.74	−0.60	−0.36
Lower clouds	A	(−0.48)	(−0.52)	(−0.26)
	B	(0.37)	(−0.03)	(0.57)
LWCF	A	−0.49	−0.66	−0.85
	B	−0.86	−0.68	−0.40
SWCF	A	(NA)	0.70	0.85
	B	(NA)	0.62	0.28
NetCRF	A	(NA)	(−0.18)	(0.36)
	B	(NA)	(−0.54)	(−0.33)

[a]Pairs of A and B with fraction of explained variance less than 73% (corresponding to a correlation coefficient less than 0.85) are placed in parentheses. TOA, top of atmosphere; OLR, outgoing long-wave radiation; TRS, total reflected solar radiation; LWCF, long-wave cloud forcing; SWCF, short-wave cloud forcing; NA, not available.

the least squares fit give an objective measure of the relative importance of PC1 and PC2 in controlling the variation within the compositing space.

[31] Table 1 shows the linear regression corresponding to Figures 4–6. Linear dependence explains most of the variance ($R^2 > 0.73$). The relative dependence on PC2 is bigger at short timescales. For example, when the timescale increases from 1 day to 5 days and 30 days, the magnitude of the correlation coefficient between anvil cloud fraction and PC2 (|B|) decreases monotonically from 0.79 to 0.39, while the dependence on PC1 (|A|) increases monotonically from 0.53 to 0.80. High-thin clouds, lower clouds and the NetCRF have the least significant response to vertical velocity. The sign of the dependence of net radiation reverses as one goes from local temporal anomalies to spatial gradients.

[32] The stronger dependence on PC2 on shorter timescales suggests that the second mode of the vertical velocity profile (PC2) mainly results from the latent heating (the stratiform type as seen in Figure 3 of *Houze* [1997]) produced by convection. When the timescale increases, impacts of radiation tend to be more important. The vertical motion associated to clear-sky radiative cooling produces a deeper mode more like EOF1 (a constant tropospheric deep cooling). Hence, we expect the relative dependence on PC1 to increase with increasing timescales.

4.4. The EP Region

[33] Composites for the EP show similar results as for the WP. Exceptions are that the composites based on climatology for the EP (not shown) have systematically less/more high-thin/lower clouds. The associated SWCF and NetCRF over the upward motion regime are more negative in the EP than in the WP, which is consistent with ISCCP and MODIS data [*Hartmann et al.*, 2001; *Kubar et al.*, 2007]. The different climatological relationship of high-thin clouds to large-scale upward motions between EP and WP suggests that, although upward motion in the upper troposphere favors high-thin clouds, other parameters rather than the strength of upward motion seem to impact the high-thin cloud (like horizontal wind field, environmental thermodynamic conditions, etc.).

4.5. Radar Rainfall Composite

[34] Here we show the dependence of shallow rain rate from PR on PC1 and PC2 derived from 2 years of PR data for the WP area. Since PR data is sparse and precipitation may change rapidly, we match PR with vertical velocity using 3-hourly averages (i.e., the PR estimate during ± 1.5 h around 00z, 06z, 12z, 18z). The composite is based on 3-hourly averaged PR rain rate and instantaneous vertical velocity. The shallow rain rate is defined as valid precipitation with radar echo top lower than 5 km. Figure 7 shows the shallow rain rate is greatest in the ''bottom heavy'' upward motion regime. Because the precipitation rates are weak, latent heating is not likely the causal factor of the strong upward motion in the lower atmosphere. The ''bottom heavy'' regime is over the relatively cold SST area in the WP region. This might suggest that strong low-level convergence tends to force convection to happen over relative cold SST. Since the thermodynamic conditions do not favor deep convection (cold SST, small CAPE, etc.) the convection tends to be shallow there. It is known that PR misses light rain rates (reflectivity <17 dbz or RR < 0.4 mm/d), so that additional light rain events are largely missed.

5. Temporal Relationships

[35] In section 4 we showed that observed clouds and radiation have significant correlation with both PC1 and

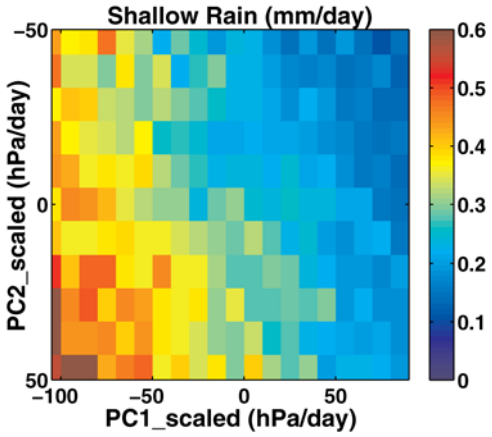

Figure 7. Shallow precipitation (precipitation radar echo top below 5 km) composited into PC1 and PC2 based on 4 × daily data. Domain used is WP, 15°S–15°N, 100°E–160°E. Time period is 1998–1999.

PC2 even on short timescales. It is interesting to investigate the temporal evolution of vertical motion and clouds associated with precipitation on short timescales. Temporal evolution of some aspects of clouds, precipitation, and dynamic properties (divergence or vertical motion profiles) during the life cycle of tropical convective systems has been previously investigated on the basis of radar and sounding measurements [e.g., *Mapes and Houze*, 1993; *Mapes et al.*, 2006]. Satellite observations provide much larger spatial samples over longer periods than ground-based measurements, and offer another way to study the temporal evolution of convection, clouds and large-scale circulation. Satellites in low Earth orbits (LEO) carrying microwave imagers, precipitation radar and visible and infrared sensors like TRMM can provide detailed retrievals of precipitation structure and more accurate properties of cloud systems. Poor sampling in time and the nighttime limit of cloud retrieving techniques make it difficult to directly study the temporal evolution of tropical convection from LEO, however. The geostationary IR radiometer is the only platform that can sample individual convective systems continuously over their entire life cycle (hours to days), but the information we can get from the IR channels is limited. Previous work utilizing geostationary satellite IR data have explored the life cycle of tropical mesoscale convective systems [e.g., *Chen and Houze*, 1997] by taking advantages of the high-frequency measurements form geostationary satellites.

[36] Here we want to explore the short-term temporal evolution of precipitation, vertical motion and cloud system associated with intense convective events using a compositing method with the help of TRMM3b42 precipitation. We composite all observed variables into a temporal reference frame and see the temporal evolution from a large number of samples rather than individual cases. We can align infrequent observational measurements to more frequent measurements by using a relative space-time frame so that we can focus on short-term process studies. To achieve this goal, we use the TRMM3b42 precipitation as the reference variable, since it has the highest temporal frequency (3-hourly) and is a reasonable index of the strength of convective systems. Second, we calculate the probability distribution of precipitation rate for precipitating grids (only counting nonzero precipitation points) over the WP. Then we choose a threshold value to select times and locations of strong convective events. We pick the highest deciles of rain rate points as reference times (the 3-h mean rate bigger than 2 mm/a).

[37] The TRMM3b42 is thus used to locate the time and location of intense precipitating events. We set as the origin each specific time and each specific location identified as containing intense precipitation. Then we composite other variables near the spatial position at times before and after that time. Composites are made for each point in a 10° × 10° area centering on the reference position.

[38] Figure 8 shows the absolute values PC1, PC2, rain fall rate, and clouds composited in space and time with respect to strong convective events in the WP. Each row shows one variable varying with time from 12 h before the event to 12 h after in 3-h intervals. The small maps show the 10° × 10° spatial region centered on the reference grid (0, 0). Bottom to top is south to north, and left to right is west to east. Note that the reference precipitation based on TRMM3b42 is an independent data set from the others used. The maximum precipitation occurs at 0 h by design, but the intense events tend to persist for 6 h or more. A small asymmetry is present with slightly more precipitation before the key time than after. This slight asymmetry is also present in the thick cloud composite, supporting the idea that the optically thick cold clouds are closely related to the production of heavy precipitation. On the other hand, the anvil clouds, which are the less optically thick cold clouds, reach their maximum abundance after the peak of precipitation. The structure of the vertical velocity is also asymmetric with respect to the precipitation event. The deep upward motion (-PC1) peaks before the precipitation event, while the top heavy upward motion (-PC2) peaks after the precipitation event. The temporal and spatial correspondence between top heavy upward motion and anvil cloud is very apparent in Figure 8.

[39] It is of interest to see if the vertical velocity anomalies and precipitation anomalies in Figure 8 are energetically consistent. As we know, the adiabatic cooling and latent heating are the major terms controlling the energy balance during intense convective events. It is interesting to simply look at how these two balance with each other during the composited short time period. Over the tropics the vertical gradients of dry static energy (ds/dz) is nearly a constant and can be given as C_p(3.3°C/km), where C_p is the specific heat of dry air at constant pressure. The vertical advection of s in the troposphere in the pressure coordinate is

$$\frac{\int_{P_0}^{P_H} \omega \frac{\partial s}{\partial p} dp}{P_0 - P_H}, \tag{7}$$

where ω, ρ g, P_0, P_H, and H are the vertical pressure velocity, air density, gravity-acceleration, surface pressure, pressure at the tropopause and the tropopause height, respectively. Then we can project two EOFs in Figure 1 on the $\frac{\partial s}{\partial p}$ profile and properly estimate the adiabatic cooling associated with the PC1 and PC2 used in this study. Since density decreases with decreasing pressure, upward motions

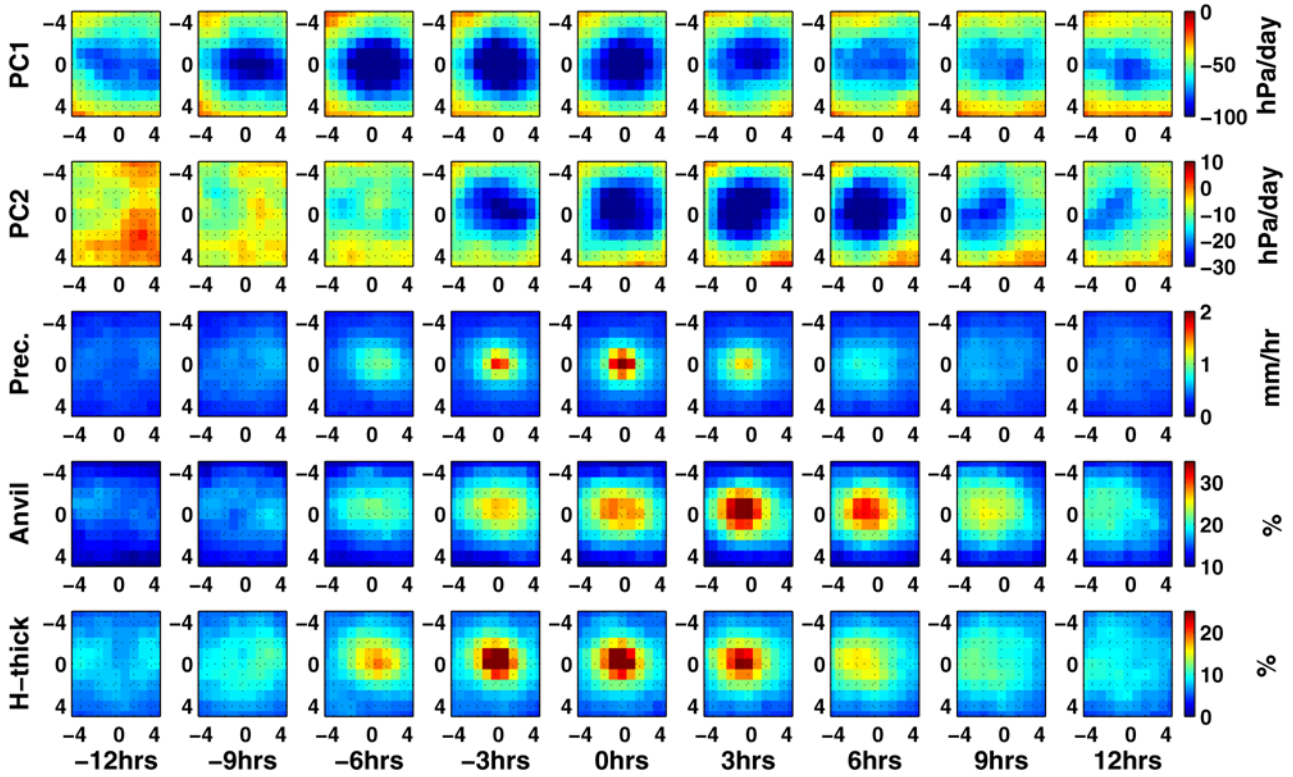

Figure 8. Temporal evolution of the vertical motion profile and clouds composited by time and space relative to strong precipitation events. Domain used is WP, 15°S–15°N, 100°E–160°E.

with the same magnitude in the upper troposphere would generate more cooling than in the lower troposphere.

[40] We use a temperature profile with surface temperature of 29°C and pressure of 1013 hPa and a lapse rate of 6.5°C/km. The estimated cooling associated with −100hPa/day of PC1 used in this study is about 396 W/m^2 (∼14.1 mm/d precipitation). The cooling associated with −100hPa/day of PC2 is about 130 W/m^2 (∼4.6 mm/d precipitation). Applying these quantities to the compositing results shown in Figure 8 within the 10° × 10° region, the area averaged variation of adiabatic cooling associated with PC1 and PC2 are ∼83 W/m^2 (−21h Pa/d) and ∼15 W/m^2 (−11.5 hPa/d), respectively. The latent heating from precipitation is ∼118 W/m^2 (4.2 mm/d). So the adiabatic cooling associated with PC1 and PC2 are ∼83% of the latent heating (98/118) observed. The 1-day integrated (−12 to +12 h) cooling and heating have the similar ratio (∼80%). When using the central 5° × 5° area, the ratio decreases to ∼51%. So for the synoptic scale (say 1000 km) the composited ERA-40 vertical motions are energetically consistent with the latent heating to within 20% or so.

[41] To have an objective view of the relative dependence of other variables on PC1 and PC2 in Figure 8, we perform a linear regression similar to that in section 4. For each variable $V(x, y, t)$ in the composited time-space frame, which "x" and "y" are the position of the box(1° × 1° size) and the "t" is the time in the composited phase space. First the temporal mean $\overline{V}_t(x, y)$ at each box is removed to get the temporal anomalies $V_t'(x, y, t)$:

$$V_t'(x,y,t) = V(x,y,t) - \overline{V}_t(x,y). \tag{8}$$

Then the temporal anomalies can be normalized:

$$V'(x,y,t) = V_t'(x,y,t)/\sigma. \tag{9}$$

The σ is the standard deviation of all the data points within the composited space:

$$\sigma = \frac{1}{N_x N_y N_t - 1} \sum_{x,y,t} \left[V_t'(x,y,t)\right]^2, \tag{10}$$

where N_x and N_y are the number of grids shown in plots at x and y direction and the number of time frames used (17, from −24 to +24 h), respectively. The least squares fits (equation (6)) are then performed on $PC1'$, $PC2'$, and V'.

[42] Figure 9 shows the regressions for the temporal variations described above. Figure 9 shows that the temporal variation of anvil clouds is well correlated with PC2. High-thick clouds and precipitation have similar temporal dependence on PC1 and PC2. Around a half of the variance can be explained by PC1 and PC2. High-thin clouds and lower clouds are less well correlated in time with PC1 and PC2.

[43] To better compare the phase information the temporal variations of normalized spatial averages of these variables are shown in Figure 10. To get the normalized temporal variations the spatial averages of each variable over the central 5° × 5° box are calculated. Then the temporal (−24–+24 h) means are removed. Finally they are divided by the amplitudes of spatial means, so that the departures of all variables are equal. Amplitudes are shown in parenthesis in legends. $\delta PC1$ and $\delta PC2$ are plotted with

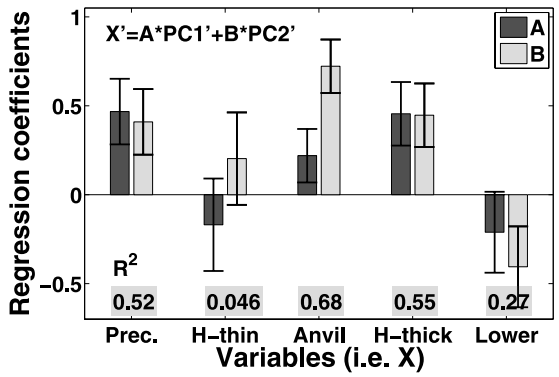

Figure 9. Relative time dependence of other variables (V') on PC1′ and PC2′ for the tropical composites in Figure 8. Error bars show 95% confidence interval based on the number of degrees of freedom. Shaded numbers are the variance explained by the least squares fit (R^2). The variables of interest are written across the bottom of the plot.

reversed sign for better comparison. Error bars show the 95% confidence interval. The autocorrelations of the data are considered to determine the number of degree of freedom [*Bretherton et al.*, 1999]. Precipitation is shown for reference in Figures 10a–10c. PC1 peaks 3 h in advance of precipitation, but PC2 lags 3 h after precipitation, which suggests that low-level convergence in advance of peak rain rate gives way to middle-level convergence afterward. This is consistent with a typical mesoscale convective system (MCS) lifecycle [*Mapes et al.*, 2006]. High-thick cloud coverage almost has the same temporal variation as precipitation, but anvils lag high-thick clouds by 3 h. The phasing of thick and anvil cloud in these observations is consistent with the observation that deep convective cloud systems evolve in time from more vigorous convective cells toward stratiform anvils with layered structure [*Houze*, 1997]. Anvil clouds and PC2 seem to have similar phasing during the intense precipitation events, which is in agreement with a recent study [*Nishi et al.*, 2007] showing that steady upper atmosphere upward motion occurs in stratiform cloud region. High-thin and lower cloud fractions vary little as precipitation changes during the strong convective system developments (not shown). Composites based on VIS clouds and TRMM PR suggest that the high-thick clouds defined in this study represent precipitating high clouds (both convective and stratiform) while the anvils defined here are more likely the weakly precipitating thick anvils (not shown).

[44] The phase differences among high-thick clouds, anvil clouds, PC1, PC2 and precipitations are robust. Composites based on different subsets of the data give similar results (not shown). Additionally PR data show that the stratiform rain rate(area fraction) lags the convective rain rate(area fraction), which is consistent with radar studies of tropical oceanic mesoscale convective systems [e.g., *Churchill and Houze*, 1984; *Houze*, 1977; *Houze and Hobbs*, 1982; *Houze and Rappaport*, 1984; *Leary*, 1984; *Wei and Houze*, 1987] (not shown). The short-term temporal co-evolution of precipitation, vertical motion and cloud system associated with intense convective events for the EP area is also investigated. The EP area results are similar to the WP area within the statistical uncertainty (not shown).

6. Conclusions and Summary

[45] Reanalysis shows that large-scale vertical velocity profiles have two significant modes that explain ~90% of the variance on all timescales. The first mode (PC1) shows a broad maximum through the middle troposphere, which is associated with the traditional deep circulation mode. The second mode (PC2) shows a shift between the upper and lower atmosphere corresponding to middle-level divergence. The second mode is found to explain more variance at shorter timescales and space scales.

[46] Despite the uncertainties inherent in vertical velocity from reanalysis, coherent relationships exist between the modes of vertical velocity derived from reanalysis and

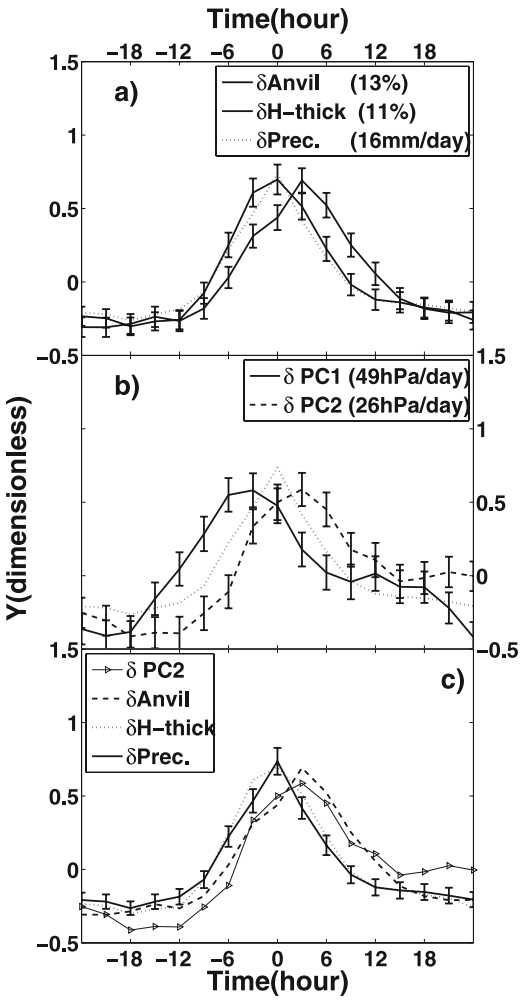

Figure 10. (a–c) Temporal evolution of the vertical motion profile and clouds composited by time and space relative to strong precipitation events in the WP. The spatial average of each variable over the central 5° × 5° box shown in Figure 9 is calculated at each time. Then the minimum value of the time series of each spatial average is subtracted. The anomaly then is scaled by dividing it with its amplitude. The negatives of δPC1 and δPC2 are plotted in order to compare the phase more easily.

cloud and radiation properties measured independently from satellites. These relationships are consistent with the evolution of cloud systems that we would expect on the basis of in situ data from field experiments conducted in the past.

[47] Composites for the western Pacific show that strong upper level large-scale ascent (''top heavy'' upward motion) is associated with deep cloud systems (more intense precipitation, lower OLR, stronger cloud long-wave forcing, and extensive anvils). Anvil cloud is sensitive to the amplitude of PC2, suggesting a strong relationship of ''top heavy'' upward motion and anvil clouds. This also supports previous work [*Hartmann et al.*, 1984; *Houze*, 1982] that the elevated heating profile produced by tropical deep convective systems results in deepening convergence in the lower troposphere.

[48] Cloud short-wave radiative forcing has weaker dependence on PC2 since short-wave effects depend upon cloud optical thickness rather than cloud top altitudes. The net cloud forcing depends more strongly on PC2 than PC1 over areas with rising motion. More net radiation goes into the area with warmest SST corresponding to ''top heavy'' upward motions and strong deep convective systems.

[49] High-thin cloud fraction shows small sensitivity to both PC1 and PC2 on short timescales, and appears to be only loosely connected to convective events [*Luo and Rossow*, 2004]. On longer timescales, high-thin clouds show stronger dependence on vertical motion and are favored by ''top heavy'' upward motion. More low clouds are found in ''bottom heavy'' regimes. The analysis shows similar results over the WP and EP region, but high-thin/lower clouds are systematically less/more in the EP than in the WP area. The difference between these two regions is consistent with results shown by ISCCP [*Hartmann et al.*, 2001] and MODIS [*Kubar et al.*, 2007] data. More shallow rain is found over the areas with ''bottom heavy'' upward motion suggesting that convection favors the area with strong low-level convergence which could moisten the lower and middle atmosphere.

[50] The co-evolution of vertical velocity and cloud properties on short timescales has also been investigated. The deep mode of vertical velocity, PC1, tends to reach its peak 3 h before intense precipitating events but PC2 reaches its peak 3 h later than precipitation. Strong upward motion tends to develop in the lower atmosphere at first and then change to the more ''top heavy'' type upward motion later during the evolution of convective events. This has been seen before from case studies using radar and sounding data [e.g., *Frank*, 1978; *Nitta*, 1977; *Ogura et al.*, 1979]. The associated cloud systems show consistent temporal changes leading from the developments of high-thick clouds to later extensive anvil clouds. High-thick clouds occur simultaneously with precipitation but anvil clouds lag 3 h behind the precipitation maximum.

[51] This study presents observed statistical relationships between cloud properties and vertical velocity profiles. These relationships could be used to diagnose/evaluate the links between large-scale dynamics and cloud properties produced by general circulation models. A potential issue is that vertical velocities from the reanalysis are not entirely observed and may be biased by the model used to make the reanalysis. Similar results to those shown here are obtained when using ERA-40 or NCEP/NCAR reanalysis products, however. It would be useful to investigate how the parameterization of diabatic processes in models used for reanalysis could bias the vertical velocity structure, but this is beyond the scope of the present work.

[52] **Acknowledgments.** This work is supported by NASA grant NNG05GA19G. CERES data were obtained from the NASA Langley Research Center EOSDIS Distributed Active Archive Center. ERA-40 was obtained from the NCAR CISL Research Data Archive. TRMM data were obtained from the NASA Goddard DAAC ftp site. The authors thank C. S. Bretherton and Robert A. Houze for useful suggestions. The authors also thank Marc Michelsen for excellent support in solving computer-related problems.

References

Awaka, J., et al. (1997), Rain type classification algorithm for TRMM precipitation radar, in *IGARSS '97: 1997 International Geoscience and Remote Sensing Symposium*, vol. 4, pp. 1633–1635, IEEE Press, Piscataway, N. J.

Back, L. (2007), Towards an improved understanding of tropical convection patterns over the oceans, Ph.D. thesis, Dep. of Atmos. Sci., Univ. of Wash., Seattle.

Back, L., and C. Bretherton (2006), Geographic variability in the export of moist static energy and vertical motion profiles in the tropical Pacific, *Geophys. Res. Lett.*, *33*, L17810, doi:10.1029/2006GL026672.

Bony, S., J.-L. Dufresne, H. Le Trout, J.-J. Morcrette, and C. Senior (2004), On dynamic and thermodynamic components of cloud changes, *Clim. Dyn.*, *22*, 71–86, doi:10.1007/s00382-003-0369-6.

Bretherton, C. S., M. Widmann, V. P. Dymnikov, J. M. Wallace, and I. Bladé (1999), The effective number of spatial degrees of freedom of a time-varying field, *J. Clim.*, *12*, 1990–2009, doi:10.1175/15200442(1999)012<1990:TENOSD>2.0.CO;2.

Cess, R. D., et al. (1989), Interpretation of cloud-climate feedback as produced by 14 atmospheric general circulation models, *Science*, *245*, 513–516, doi:10.1126/science.245.4917.513.

Chen, S. S., and J. R. A. Houze (1997), Diurnal variation and life cycle of deep convective systems over the tropical Pacific warm pool, *Q. J. R. Meteorol. Soc.*, *123*, 357–388, doi:10.1002/qj.49712353806.

Churchill, D. D., and R. A. Houze (1984), Mesoscale updraft magnitude and cloud-ice content deduced from the ice budget of the stratiform region of a tropical cloud cluster, *J. Atmos. Sci.*, *41*, 1717–1725, doi:10.1175/1520-0469(1984)041<1717:MUMACI>2.0.CO;2.

Dhuria, H. L., and H. L. Kyle (1990), Cloud types and the tropical earth radiation budget, *J. Clim.*, *3*, 1409–1434, doi:10.1175/1520-0442(1990)003<1409:CTATTE>2.0.CO;2.

Doelling, D. R., et al. (2006), The newly released 5-year Terra-based monthly CERES radiative flux and cloud product, paper presented at 12th Conference on Atmospheric Radiation, Am. Meteorol. Soc., Madison, Wis.

Dong, X., G. G. Mace, P. Minnis, W. L. Smith Jr., M. Poellot, R. T. Marchand, and A. D. Rapp (2002), Comparison of stratus cloud properties deduced from surface, GOES, and aircraft data during the March 2000 ARM Cloud IOP, *J. Atmos. Sci.*, *59*, 3265–3284, doi:10.1175/1520-0469(2002)059<3265:COSCPD>2.0.CO;2.

Folkins, I., S. Fueglistaler, G. Lesins, and T. Mitovski (2008), A low-level circulation in the tropics, *J. Atmos. Sci.*, *65*, 1019–1034.

Frank, W. M. (1978), The life cycles of GATE convective systems, *J. Atmos. Sci.*, *35*, 1256–1264, doi:10.1175/1520-0469(1978)035<1256:TLCOGC>2.0.CO;2.

Frank, W. M., and J. L. McBride (1989), The vertical distribution of heating in AMEX and GATE cloud clusters, *J. Atmos. Sci.*, *46*, 3464–3478, doi:10.1175/1520-0469(1989)046<3464:TVDOHI>2.0.CO;2.

Hartmann, D. L., H. H. Hendon, and R. A. Houze Jr. (1984), Some implications of the mesoscale circulations in tropical cloud clusters for large-scale dynamics and climate, *J. Atmos. Sci.*, *41*, 113–121, doi:10.1175/1520-0469(1984)041<0113:SIOTMC>2.0.CO;2.

Hartmann, D. L., M. E. Ockert-Bell, and M. L. Michelsen (1992), The effect of cloud type on Earth's energy balance: Global analysis, *J. Clim.*, *5*, 1281–1304, doi:10.1175/1520-0442(1992)005<1281:TEOCTO>2.0.CO;2.

Hartmann, D. L., L. A. Moy, and Q. Fu (2001), Tropical convection and the energy balance at the top of the atmosphere, *J. Clim.*, *14*, 4495–4511, doi:10.1175/1520-0442(2001)014<4495:TCATEB>2.0.CO;2.

Houze, R. A. (1977), Structure and dynamics of a tropical squall-line system, *Mon. Weather Rev.*, *105*, 1540–1567, doi:10.1175/1520-0493(1977)105<1540:SADOAT>2.0.CO;2.

Houze, R. A. (1982), Cloud clusters and large-scale vertical motions in the Tropics, *J. Meteorol. Soc. Jpn.*, *60*, 396–410.

Houze, R. A. (1989), Observed structure of mesoscale convective systems and implications for large-scale heating, *Q. J. R. Meteorol. Soc.*, *115*, 425–461, doi:10.1002/qj.49711548702.

Houze, R. A., Jr. (1997), Stratiform precipitation in regions of convection: A meteorological paradox?, *Bull. Am. Meteorol. Soc.*, *78*, 2179–2196, doi:10.1175/1520-0477(1997)078<2179:SPIROC>2.0.CO;2.

Houze, R. A., and P. V. Hobbs (1982), Organization and structure of precipitating cloud systems: Advances in Geophysics, *Adv. Geophys.*, *24*, 225–315.

Houze, R. A., and E. N. Rappaport (1984), Air motions and precipitation structure of an early summer squall line over the eastern tropical Atlantic, *J. Atmos. Sci.*, *41*, 553–574, doi:10.1175/1520-0469(1984)041<0553:AMAPSO>2.0.CO;2.

Huffman, G. J. (1997), Estimates of root-mean-square random error for finite samples of estimated precipitation, *J. Appl. Meteorol.*, *36*, 1191–1201, doi:10.1175/1520-0450(1997)036<1191:EORMSR>2.0.CO;2.

Huffman, G. J., R. F. Adler, B. Rudolf, U. Schneider, and P. R. Keehn (1995), Global precipitation estimates based on a technique for combining satellite-based estimates, rain gauge analysis, and NWP model precipitation information, *J. Clim.*, *8*, 1284–1295, doi:10.1175/1520-0442(1995)008<1284:GPEBOA>2.0.CO;2.

Huffman, G. J., et al. (1997), The Global Precipitation Climatology Project (GPCP) combined precipitation dataset, *Bull. Am. Meteorol. Soc.*, *78*, 5–20, doi:10.1175/15200477(1997)078<0005:TGPCPG>2.0.CO;2.

Iguchi, T., T. Kozu, R. Meneghini, J. Awaka, and K. Okamoto (2000), Rain-profiling algorithm for the TRMM precipitation radar, *J. Appl. Meteorol.*, *39*, 2038–2052, doi:10.1175/1520-0450(2001)040<2038:RPAFTT>2.0.CO;2.

Intergovernmental Panel on Climate Change (2007), *Climate Change 2007: The Physical Science Basis*, 800 pp., Cambridge Univ. Press, New York.

Johnson, R. H., T. M. Rickenbach, S. A. Rutledge, P. E. Ciesielski, and W. H. Schubert (1999), Trimodal characteristics of tropical convection, *J. Clim.*, *12*, 2397–2418, doi:10.1175/1520-0442(1999)012<2397:TCOTC>2.0.CO;2.

Kubar, T. L., D. L. Hartmann, and R. Wood (2007), Radiative and convective driving of tropical high clouds, *J. Clim.*, *20*, 5510–5526, doi:10.1175/2007JCLI1628.1.

Leary, C. A. (1984), Precipitation structure of the cloud clusters in a tropical easterly wave, *Mon. Weather Rev.*, *112*, 313–325, doi:10.1175/1520-0493(1984)112<0313:PSOTCC>2.0.CO;2.

Lin, J., B. E. Mapes, M. Zhang, and M. Newman (2004), Stratiform precipitation, vertical heating profiles, and the Madden–Julian oscillation, *J. Atmos. Sci.*, *61*, 296–309, doi:10.1175/1520-0469(2004)061<0296:SPVHPA>2.0.CO;2.

Luo, Z., and W. Rossow (2004), Characterizing tropical cirrus life cycle, evolution, and interaction with upper-tropospheric water vapor using Lagrangian trajectory analysis of satellite observations, *J. Clim.*, *17*, 4541–4563, doi:10.1175/3222.1.

Mapes, B. E., and R. A. Houze (1993), An integrated view of the 1987 Australian monsoon and its mesoscale convective systems: II. Vertical structure, *Q. J. R. Meteorol. Soc.*, *119*, 733–754.

Mapes, B. E., and R. A. Houze (1995), Diabatic divergence profiles in western Pacific mesoscale convective systems, *J. Atmos. Sci.*, *52*, 1807–1828, doi:10.1175/1520-0469(1995)052<1807:DDPIWP>2.0.CO;2.

Mapes, B., S. Tulich, J. Lin, and P. Zuidema (2006), The mesoscale convection life cycle: Building block or prototype for large-scale tropical waves?, *Dyn. Atmos. Oceans*, *42*, 3–29, doi:10.1016/j.dynatmoce.2006.03.003.

Minnis, P., et al. (1995), Cloud optical property retrieval (subsystem 4.3), in *Clouds and the Earth's Radiant Energy System (CERES) Algorithm Theoretical Basis Document*, vol. 3, *Cloud Analyses and Radiance Inversions (Subsystem 4)*, *NASA Ref. Publ., NASA RP-1376*, 135–176.

Minnis, P., et al. (1999), Cloud properties derived from CERES for VIRS, paper presented at 10th Conference on Atmospheric Radiation, Am. Meteorol. Soc., Madison, Wis.

Nishi, N., M. K. Yamamoto, T. Shimomai, A. Hamada, and S. Fukao (2007), Fine structure of vertical motion in the stratiform precipitation region observed by a VHF Doppler radar installed in Sumatra, Indonesia, *J. Appl. Meteorol. Climatol.*, *46*, 522–537, doi:10.1175/JAM2480.1.

Nitta, T. (1977), Response of cumulus updraft and downdraft to GATE A/B-scale motion systems, *J. Atmos. Sci.*, *34*, 1163–1186, doi:10.1175/1520-0469(1977)034<1163:ROCUAD>2.0.CO;2.

Ockert-Bell, M. E., and D. L. Hartmann (1992), The effect of cloud type on Earth's energy balance: Results for selected regions, *J. Clim.*, *5*, 1157–1171, doi:10.1175/1520-0442(1992)005<1157:TEOCTO>2.0.CO;2.

Ogura, Y., Y.-L. Chen, J. Russell, and S.-T. Soong (1979), On the formation of organized convective systems observed over the eastern Atlantic, *Mon. Weather Rev.*, *107*, 426–441, doi:10.1175/1520-0493(1979)107<0426:OTFOOC>2.0.CO;2.

Pandya, R., and D. Durran (1996), The influence of convectively generated thermal forcing on the mesoscale circulation around squall lines, *J. Atmos. Sci.*, *53*, 2924–2951, doi:10.1175/1520-0469(1996)053<2924:TIOCGT>2.0.CO;2.

Ramanathan, V., and W. Collins (1991), Thermodynamic regulation of ocean warming by cirrus clouds deduced from observations of the 1987 El-Nino, *Nature*, *351*, 27–32, doi:10.1038/351027a0.

Reed, R. J., and E. E. Recker (1971), Structure and properties of synoptic-scale wave disturbances in the equatorial western Pacific, *J. Atmos. Sci.*, *28*, 1117–1133, doi:10.1175/1520-0469(1971)028<1117:SAPOSS>2.0.CO;2.

Schumacher, C., R. A. Houze Jr., and I. Kraucunas (2004), The tropical dynamical response to latent heating estimates derived from the TRMM precipitation radar, *J. Atmos. Sci.*, *61*, 1341–1358, doi:10.1175/1520-0469(2004)061<1341:TTDRTL>2.0.CO;2.

Stephens, G. L. (2005), Cloud feedbacks in the climate system: A critical review, *J. Clim.*, *18*, 237–273, doi:10.1175/JCLI-3243.1.

Thompson, R. M., S. W. Payne, E. E. Recker, and R. J. Reed (1979), Structure and properties of synoptic-scale wave disturbances in the Intertropical Convergence Zone of the Eastern Atlantic, *J. Atmos. Sci.*, *36*, 53–72, doi:10.1175/1520-0469(1979)036<0053:SAPOSS>2.0.CO;2.

Trenberth, K., D. P. Stepaniak, and J. M. Caron (2000), The global monsoon as seen through the divergent atmospheric circulation, *J. Clim.*, *13*, 3969–3993, doi:10.1175/1520-0442(2000)013<3969:TGMAST>2.0.CO;2.

Uppala, S. M., et al. (2005), The ERA-40 re-analysis, *Q. J. R. Meteorol. Soc.*, *131*, 2961–3012.

Wei, T., and R. A. Houze Jr. (1987), The GATE squall line of 9–10 August 1974, *Adv. Atmos. Sci.*, *4*, 85–92.

Wielicki, B. A., B. R. Barkstrom, E. F. Harrison, R. B. Lee III, G. Louis Smith, and J. E. Cooper (1996), Clouds and the Earth's Radiant Energy System (CERES): An Earth observing system experiment, *Bull. Am. Meteorol. Soc.*, *77*, 853–868, doi:10.1175/1520-0477(1996)077<0853:CATERE>2.0.CO;2.

Williams, K. D., et al. (2003), Evaluating the cloud response to climate change and current climate variability, *Clim. Dyn.*, *20*, 705–721.

Wyant, M., et al. (2006), A comparison of low-latitude cloud properties and their response to climate change in three AGCMs sorted into regimes using mid-tropospheric vertical velocity, *Clim. Dyn.*, *27*, 261–279, doi:10.1007/s00382-006-0138-4.

Yuan, J., D. L. Hartmann, and R. Wood (2008), Dynamic effects on the tropical cloud radiative forcing and radiation budget, *J. Clim.*, *21*, 2337–2351.

Zhang, C., M. McGauley, and N. A. Bond (2004), Shallow meridional circulation in the tropical eastern Pacific, *J. Clim.*, *17*, 133–139, doi:10.1175/1520-0442(2004)017<0133:SMCITT>2.0.CO;2.

D. L. Hartmann and J. Yuan, Department of Atmospheric Sciences, University of Washington, Seattle, WA 98195, USA. (jiany@atmos.washington.edu)